



**HAL**  
open science

# Implementation of an Optical Measurement Method for Monitoring Mechanical Behaviour

Arthur Bontemps, Gaël Godi, Eric Fournely, Rostand Moutou Pitti, Joseph Gril

► **To cite this version:**

Arthur Bontemps, Gaël Godi, Eric Fournely, Rostand Moutou Pitti, Joseph Gril. Implementation of an Optical Measurement Method for Monitoring Mechanical Behaviour. *Experimental Techniques*, 2024, 48 (1), pp.115-128. <10.1007/s40799-023-00636-2>. <hal-04095871>

**HAL Id: hal-04095871**

**<https://hal.science/hal-04095871v1>**

Submitted on 12 May 2023

**HAL** is a multi-disciplinary open access archive for the deposit and dissemination of scientific research documents, whether they are published or not. The documents may come from teaching and research institutions in France or abroad, or from public or private research centers.

L'archive ouverte pluridisciplinaire **HAL**, est destinée au dépôt et à la diffusion de documents scientifiques de niveau recherche, publiés ou non, émanant des établissements d'enseignement et de recherche français ou étrangers, des laboratoires publics ou privés.



HAL Authorization

# Implementation of an optical measurement method for monitoring mechanical behaviour

Arthur Bontemps<sup>1\*</sup>, Gaël Godi<sup>1</sup>, Eric Fournely<sup>1</sup>, Rostand Moutou Pitti<sup>1,2</sup> and Joseph Gril<sup>1,3</sup>

<sup>1</sup>\*Université Clermont Auvergne, Clermont Auvergne INP, CNRS, Institut Pascal, F-63000 Clermont-Ferrand, France..

<sup>2</sup>CENAREST, IRT, BP 14070, Libreville, Gabon.

<sup>3</sup>Université Clermont Auvergne, INRAE, PIAF, F-63000 Clermont Ferrand, France.

\*Corresponding author(s). E-mail(s): [arthur.bontemps@uca.fr](mailto:arthur.bontemps@uca.fr);  
Contributing authors: [gael.godi@uca.fr](mailto:gael.godi@uca.fr); [eric.fournely@uca.fr](mailto:eric.fournely@uca.fr);  
[rostand.moutou-pitti@uca.fr](mailto:rostand.moutou-pitti@uca.fr); [joseph.gril@cnrs.fr](mailto:joseph.gril@cnrs.fr);

## Abstract

There is a gap between mechanical measurement methods under laboratory conditions and those under real conditions of structural monitoring. This paper proposes a method that applies well-established computer vision developments to photomechanics in difficult conditions. It is therefore a technique that is flexible and versatile while maintaining satisfying accuracy. It consists in marker tracking using ArUco fiducial markers as measurement points. It allows locating markers in non-optimal conditions of camera orientation and position. A homography process was used to analyse pictures taken with a view angle. The accuracy of the method was estimated, especially in case of out-of-plane motions, and the impact of the view angle and of the distance between camera and markers on the location error was studied. The method was applied in creep tests to measure crack parameters as well as the transverse expansion of wooden beams. In the application example presented, it enabled to compute distances between markers with only 0.28% of relative error and hence to measure the crack parameters and the long-term shrinkage-swelling of the wooden beams. However, the impacts of brightness variations and camera parameters have not been estimated. This method is very promising when experimental conditions are variable and when multiple measurements are necessary.

**Keywords:** Marker tracking, crack monitoring, timber, homography, fiducial markers

## Nomenclature

$U$	Zero-order tensor $U$ , a scalar.
$\underline{U}$	First order tensor $U$ , a vector.
$\underline{\underline{U}}$	Second order tensor $U$ , a matrix.
$\underline{\underline{A}}$	Homography resolution matrix.
$\overline{CL}$	Crack length.
CO	Crack opening.
$D$	Distance between camera and calibration target.
dy12	y distance between markers 1 and 2, 40 mm apart.
dy34	y distance between markers 3 and 4, 175 mm apart.
dx12	x distance between markers 1 and 2, should be 0 mm.
dx34	x distance between markers 3 and 4, should be 0 mm.
EMC	Equilibrium moisture content.
$\underline{H}$	Homography matrix.
$H_{p1}, H_{p2}$	Distance between markers in calibration target's plane, in beam's plane.
$h_{ij}$	Homography matrix components.
$\hat{h}_{ij}$	Homography matrix components divided by $h_{33}$ .
ht, wt	Index of use of respectively horseshoe target marker and window target.
$L_0$	Initial length of a calibration target.
$\underline{X}$	Real world coordinates vector.
$X, Y, Z$	Real world coordinates components.
$\underline{\hat{X}}$	Real world coordinates vector divided by $Z$ .
$\hat{x}, \hat{y}$	Real world coordinates components divided by $Z$ .
$\underline{x}$	Homogeneous 2D image coordinates vector.
$x, y$	Homogeneous 2D image coordinates components.
$\alpha_{al}$	Thermal expansion coefficient of aluminium.
$\Delta L$	Length variation of a calibration target.
$\Delta T$	Temperature variation.
$\omega$	Scale factor.

## 1 Introduction

In experimental mechanics, measurements by optical methods are increasingly common. The main optical methods are: marker tracking; digital image correlation (DIC); grid method, photoelasticimetry; moiré; interferometry [1]. These methods are very accurate and are among the only ones that can be used to perform full-field measurements [2]. Obviously, DIC or grid method are more powerful than the marker tracking. Most of the time, both the marker tracking and the DIC are realised under controlled and restrictive conditions. The lightening conditions, the temperature of the room and the

camera positions are controlled, allowing a high accuracy for the measurement of mechanical parameters. But these conditions are rarely found in the monitoring of actual structures, making these methods unsuitable.

On the other hand, the computer vision community develops increasingly efficient methods for camera pose estimation [3]. Augmented reality or robot navigation are examples among others. Efforts have recently been made by some authors to introduce the development of computer vision into photomechanics, such as planar markers for the monitoring of crack patterns in historic structures with a camera of UAVs [4], or an image processing technique for automatic crack monitoring using homography and circular grid onto concrete object [5].

This paper is another attempt to use fiducial markers in mechanical measurements. With a need for a flexible and polyvalent method for monitoring crack propagation in wooden beams, an adapted marker tracking technique has been developed. This method uses the development of computer vision algorithms to increase marker location accuracy. Moreover, fiducial markers are unique and differentiable, allowing to measure large displacements. A homography process ensures reliable measurements while the camera is moving. Settings and application examples of the method in creep tests on wood will be described. This paper does not aim at analysing creep tests results, but at showing how this method may be used.

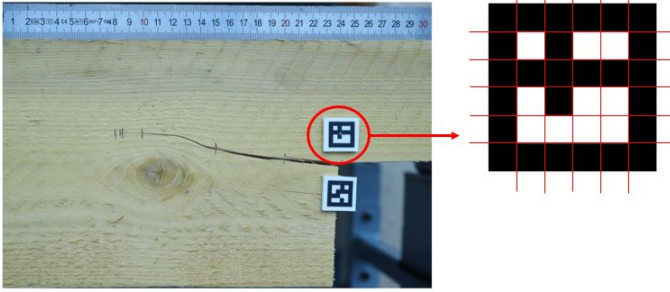
## 2 Material and methods

### 2.1 Preparation

This tracking technique uses ArUco (Augmented Reality University of Córdoba) markers, developed in Spain in 2013 and common in computer vision applications but employed here as a tool to measure relative displacements. It consists in sticking markers on the surface of an object (e.g., a beam) and taking pictures of a portion of that object containing the marker. The marker follows the point where it is glued and by measuring the position of this marker in a photo, the relative position of the considered point can be calculated. The marker detection in a picture is illustrated in Figure 1.

#### 2.1.1 ArUco markers and OpenCV library

Fiducial markers are reference objects placed in the field of view of the camera when an image or video frame is captured. ArUco markers are a specific type of fiducial markers, consisting of a black square with a white foreground that has been generated in a particular pattern (Figure 1). The black border surrounding the marker makes it easier for computer vision and image processing algorithms to detect it in a variety of scenarios, including variations in rotation, scale and lightening conditions. It looks like a QR code: a 2D binary pattern that can be detected using computer vision algorithms. ArUco

4 *An ArUco marker tracking method*

**Fig. 1** Detection of ArUco markers stuck on a notched beam. An ArUco marker is a  $6 \times 6$  matrix of black or white squares.

markers were chosen since they are reliable, versatile and their recognition is very fast and easy [6].

Throughout this study the markers are  $18 \times 18$  mm, printed on standard paper with a printer Sharp MX-3051 and protected by matt lamination in order to avoid reflection and humidity degradation. A comparison between markers location on a regular paper and on a laminated paper showed that the lamination process did not affect the marker position.

The ArUco markers are integrated in OpenCV (Open source Computer Vision), an open-source library of computer vision algorithms, written in python and C++. The ArUco module that was affected here contains functions allowing to import and print the markers, detect them in a picture and many other actions. More information about the available functions can be obtained in OpenCV website.

In the present study the following configuration was used:

- Python 3.8.5;
- Anaconda environment;
- OpenCV 4.5.2.52.

The ArUco markers were detected using the detectMarkers function of OpenCV, using default parameters; the detection process is documented in [6]. Each marker has its own pattern so that it can be identified separately from the others.

To improve the detection precision, the cornerSubPix method of OpenCV was used. The subpix function process is described in [7]. The centers of the markers are interpolated from the corners returned by the previous functions. This detection procedure ensures a much better precision than one pixel. Many other functions are available in OpenCV, e.g., calibrateCamera, findHomography.

### 2.1.2 The homography process and the calibration targets

When a photo is captured, it is necessary to compute the real distance between markers. Therefore, a reference is needed to convert pixel distance into metric distance. For this purpose, the homography process is used, as explained in Appendix A. It consists in projecting the image plane into the intended metric plane, through the homography matrix  $\underline{\underline{H}}$  that converts distances and allows taking pictures with a view angle.

$$\underline{\underline{H}} = \begin{bmatrix} h_{11} & h_{12} & h_{13} \\ h_{21} & h_{22} & h_{23} \\ h_{31} & h_{32} & h_{33} \end{bmatrix} \quad (1)$$

This homography matrix is computed using a calibration target, which is a reference object composed here of 4 ArUco markers stuck onto an aluminium object and with known relative distances. Every photo has to contain this calibration target in order to perform the projection and compute the distance between the markers. The thickness of the calibration target and that of the rigid body where the markers are stuck are the same, in order to have all markers placed in the same plane. Two calibration targets were created: a horseshoe target and a window target (Figure 2). The input dimensions for the printer is presented in Figure 2 but their exact dimensions, checked by taking a zoomed-picture of the printed target next to a ruler, was : window target, 211.3 mm  $\times$  181.5 mm; horseshoe target, 74 mm  $\times$  73.5 mm.

These aluminium calibration targets are only subjected to temperature variations due to outdoor conditions. As the linear thermal expansion coefficient of aluminium is  $\alpha_{al} = 23 \times 10^{-6} \text{ K}^{-1}$ , a temperature variation  $\Delta T = 60 \text{ K}$  (the maximum expected in a whole year), for the length  $L_0 = 210 \text{ mm}$  of the window target, induced a length variation:

$$\Delta L = \alpha_{al} L_0 \Delta T = 0.29 \text{ mm} \quad (2)$$

and for the 74 mm of the horseshoe target:  $\Delta L = 0.102 \text{ mm}$ . As the markers of the calibration targets are stuck onto the aluminium with superglue, it was worth checking if the adhesive expands with the aluminium. A climate chamber was used to apply a  $\Delta T = 70 \text{ K}$  on an aluminium calibration target and its dimensions was measured with another calibration target of control. The experimental thermal coefficient determined with this setup was  $22 \times 10^{-6} \text{ K}^{-1}$ . This value, close to the theoretical one, proved that the markers follow the material subjected to thermal expansion. As a consequence, the thermal expansion has a significant effect on the calibration target's dimensions and requires a correction.

The two calibration targets were adapted to different ranges. The horseshoe and the window measured distance variations between markers initially 4 cm and 17.5 cm apart, respectively. It was considered that the closer the dimension

to the target distance, the better the precision.

Note that when a picture is taken, the top-left marker of the calibration target used is taken as origin. Therefore, each picture has its own local coordinate system relative to the position of the calibration target.

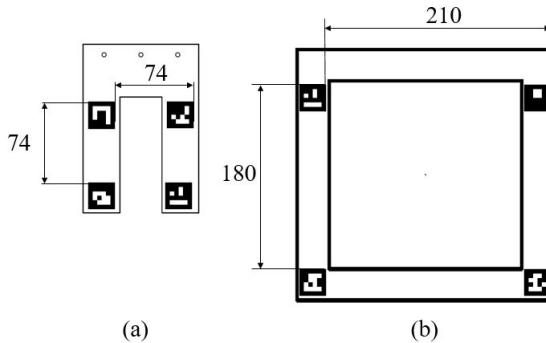


**Fig. 2** Drawing of the calibration target: (a) the horseshoe target and (b) the window target. Numerical values are in millimeters.

## 2.2 Feasibility tests

The main camera used in this study is a Canon EOS 1D X Mark II:  $5472 \times 3648$  pixels. It is a Single Lens Reflex (SLR) camera with CMOS (Complementary Metal Oxide Semiconductor) sensor. For all the photos taken in the context of this study, the parameters used were:

- Fixed focal length 50 mm;
- ISO varying from 1000 to 4000, depending on the outside light;
- Aperture F6.3;
- Autofocus activated;
- Shutter speed varying depending on the outside light.

As autofocus is activated and ISO and shutter speed are varying, no distortion correction is applied. Indeed this needs a camera calibration that is only efficient when the last mentioned parameters are constant. It was not conceivable to compute camera calibration and correct distortion at each picture because the method aims to be flexible and simple. Besides, for a 50 mm fixed-focal length distortions remain very low and only affect the border of a picture.

In every case, the gray scale between the markers and the surrounding white border is estimated. The goal is to check that the gray scale gradient is as large as possible but without reaching saturation (i.e., a gray scale of 255 or 0 for the pixels around the markers). In order to provide this information for the analysis, all graphic captions contain three data:

- Diffgray, average gray scale gradient between black and white of all pictures of the running test; it should be as large as possible;

- Mingray, minimum gray scale level reached among all pictures of the running test; it should be above 0;
- Maxgray, maximum gray scale level reached among all pictures of the running test; it should be below 255.

### 2.2.1 Test on a paper sheet

To validate the method in laboratory conditions, pictures of a paper sheet containing ArUco markers were taken (Figure 3). The distance between the markers was known. Some markers were used for the homography and some were used as subject to check if the distance between them was correctly computed.

In Figure 3, two calibration targets were used: markers 10, 11, 12, 13 (square of

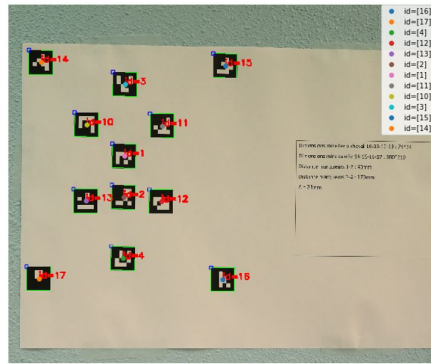


**Fig. 3** Photo of a paper sheet containing ArUco markers taken with the Canon camera. Markers 1 and 2 are 40 mm apart, markers 3 and 4 are 175 mm apart. Markers 10, 11, 12, 13 form a square of 74 mm and markers 14, 15, 16, 17 form a rectangle of  $210 \times 180$  mm.

74 mm) stand for the horseshoe and markers 14, 15, 16, 17 (rectangle of  $210 \times 180$  mm) for the window. The distance between markers 1 and 2 (40 mm), as well as that between markers 3 and 4 (175 mm) were computed using both the horseshoe and the window target. These distances were chosen because they correspond to the distance measured during the application of this method.

This paper sheet was photographed with two cameras: the Canon camera (20 MPx) and a smartphone Fairphone 3 (12 MPx). For both cameras 20 photos were taken at the same distance from the paper sheet: 120 cm. No tripod was used. The first results show a quite good accuracy, Table 1. As expected, the Canon camera is more reliable than the Fairphone 3 camera regarding the standard deviation. The dispersion is around 10 times lower and the result is closer to the true value for 40 mm. This difference may come from multiple parameters such as the photo resolution or the manufacturing quality.

**Table 1** Results for 20 photos taken with two cameras: a smartphone camera and a Canon SLR camera. Gray scale: diffgray = 155, mingray = 18, maxgray = 190

		Markers 1-2	Markers 3-4
smartphone Fairphone 3	mean y distance [mm]	39.984	175.019
	standard deviation [mm]	0.026	0.033
Canon camera	mean y distance [mm]	40.002	175.034
	standard deviation [mm]	0.002	0.003

### 2.2.2 Test in real conditions

The next step was to check the feasibility in real conditions. A 4-point bending test was conducted until failure on a notched wooden beam of silver fir (*Abies alba*). The method was used for measuring the crack opening, by computing the positions of the 2 markers stuck onto the notch where the crack was expected to occur. The position of the two markers was converted into a distance with a homography using the horseshoe target. The variation of x distance between the two markers yields the crack opening in mode II (sliding) and the y distance that in mode I (separation). The curvature of the beam does not impact the distances because the local coordinate system rotates with the beam. The thickness of the calibration targets being 3 mm, the markers were also glued on a 3 mm thick PLA (Poly-Lactic Acid) support so that they were in the same plane.

The bending test was carried out respecting the norm NF EN 408+A1 [8] and controlled in displacement. Every 2 mm imposed, or each time a crack was heard or observed, a series of 5 to 10 photos were taken to estimate the crack opening at the imposed displacement. Computing the mean of the 10 photos decreases the random uncertainties by reducing the dispersion. The photos were taken with two cameras: the Canon camera and a smartphone Asus X00TD Zenfone Max (12 MPx), Figure 4.

Figure 4 shows the measurements of the crack opening at each stage of the test. Each point represents the result of a photo. The graph clearly shows that the Canon camera gives much less dispersed results than the Asus camera.

The beam cracked at the 6th step, when the central deflection exceeded 20 mm.

## 2.3 Precision and application example

### 2.3.1 Effect of the angle and of the distance between camera and markers

As the method was planned to be used from different shooting positions, the impact of the observation angle and of the distance between camera and markers was estimated.

The effect of the distance, affecting the marker size in a picture (i.e., in pixels), was estimated using the same paper sheet (Figure 3). It was placed in front of the camera, which was moved back from 40 cm to 200 cm by steps of 10 cm, Figure 5. Five pictures were taken at each step.

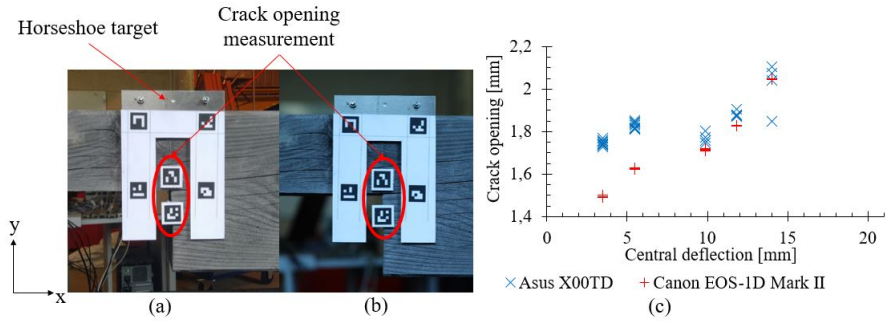


**Fig. 4** Crack opening measurement: (a) photo taken with the smartphone Asus; (b) photo taken with the Canon camera; (c) results of crack opening as a function of the central deflection imposed, left side of the beam. Gray scale:  $\text{diffgray} = 171$ ,  $\text{mingray} = 37$ ,  $\text{maxgray} = 248$ .

The effect of the observation angle was estimated with the camera placed on

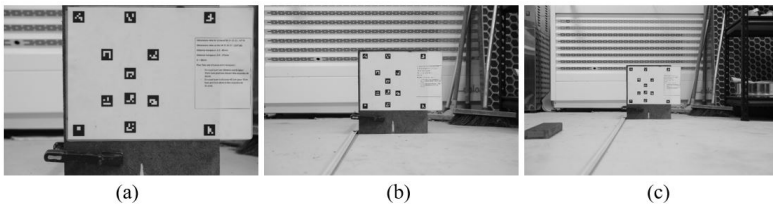


**Fig. 5** Photos taken for the estimation of the impact of distance between camera and target. (a) camera 60 cm from the target; (b) 130 cm; (c) 200 cm.

a tripod at 90 cm from the paper sheet (Figure 3). To simulate different view angles, the target was rotated around a vertical axis, then turned by  $90^\circ$  and rotated again, Figure 6. The paper sheet was rotated from  $0$  to  $45^\circ$  by steps of  $5^\circ$ . Ten pictures were taken at each step.

### 2.3.2 Application to creep tests

The method was then employed for the monitoring of long-term tests. The experimental campaign aimed at gaining a better understanding of long-term mechanical evolution, the delayed mechanical response of green or partially dried silver fir wood, coupled with crack propagation. Creep tests were performed in 4-points bending on notched wooden beams in outdoor sheltered conditions. The beams were  $4000 \times 175 \times 63$  mm and were notched at both ends like in the previous test, in order to trigger fracture initiation during the creep. Six beams were loaded at a time, by series of three spaced 50 cm from each other (Figure 7a). Three campaigns of multi-step creep tests were conducted, each lasting 4 to 6 months, with an initial load of around 350 kg subsequently increased by steps using additional weights. The first started in May 2021, the second in October 2021, the third in April 2022. Global

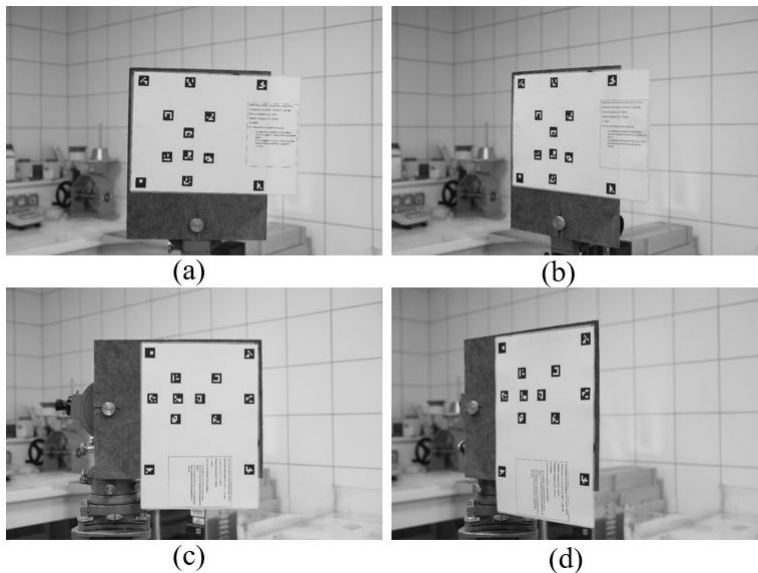


**Fig. 6** Photos taken to estimate the impact of an angle. (a) camera straight in front of the target; (b) vertical angle of 45°; (c) camera straight in front of the target turned 90°; (d) horizontal angle of 45°, simulated by the 90° turn of the target.

movements of the beam, such as central or lateral deflections, were recorded using linear variable differential transducers (LVDT) placed under the beams. However, a large number of local data such as crack propagation or height variations due to moisture-induced expansion were also needed and not so easily obtained using conventional sensors (e.g., strain gauges, digital image correlation, linear transducers), due to outdoor conditions, limited available space and limited available devices. ArUco method has been tried as an alternative, owing to its flexibility.

In order to resist to outdoor conditions, the markers were stuck using superglue onto a PLA support, 3 mm thick as well so that the calibration targets and the markers on the PLA are placed in the same plane.

As the calibration targets are subjected to outdoors conditions, a temperature correction was applied using the thermal expansion of aluminium  $23 \times 10^{-6} \text{ K}^{-1}$  and the outside temperature measured by the weather station close to the experiment.

During the creep tests the shrinkage-swelling, crack opening, length and height were measured with the method (Figure 7b). The crack opening was measured with the same scheme as the 4-points bending tests, i.e. the distance between two markers placed on the notch. The crack length and height (CL, CH) refer to the crack tip position in comparison to the markers placed at the notch, the one used for crack opening measurements. The crack tip position

is measured by positioning a marker at the eyed-observed end of the crack. Hence CL and CH refer respectively to the horizontal and vertical distances between the crack tip marker and the marker on the notch. Considering that the markers on the notch are only subjected to transverse translation (i.e. neglecting the longitudinal dilatation and the crack opening in mode 2), they were a static reference for the crack length. The tip marker was placed with magnetic tape to a removable slit in steel. Both the marker and the slit could be moved. The horseshoe target was used for this measurement because the distance between the markers is of the same order of magnitude as the distance between the markers used for the crack opening measurement. The shrinkage-swelling (or transverse expansion) of wood was measured with two markers placed at the extremity of the beam's height. Indeed, the wood is a hygroscopic material whose dimensions are in balance with its environment. If the beam shrinks, the transverse expansion is negative and if it swells, the transverse expansion is positive. During the first campaign, twelve pairs of markers per beam were used for this measurement: on each of the four sides (face 1 left, face 1 right, face 2 left and face 2 right), three couples spaced 30, 60 and 90 cm from the notch. During the second and third campaign, six pairs of markers were used: at the left, the middle and the right of the two faces of each beam. The window target was used for this measurement because the distance between the markers is of the same order of magnitude as the distance between the markers used for this measurement.

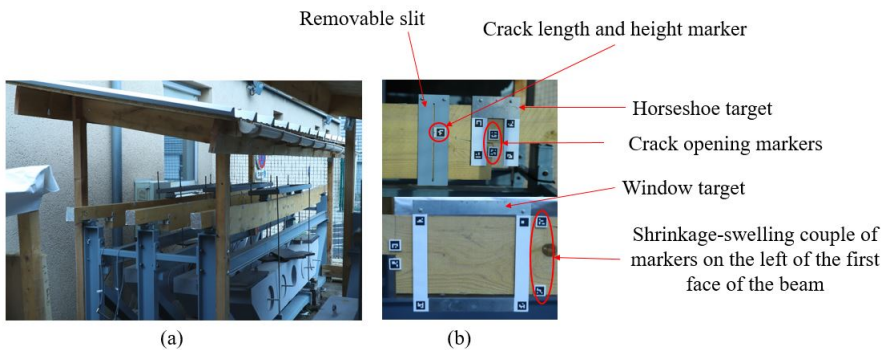


**Fig. 7** Configuration of the creep tests: (a) Illustration of creep tests of three notched beams, (b) ArUco markers measurements.

### 2.3.3 Effect of the out-of-plane displacement

Wood is a hygroscopic material that may shrink and warp if subjected to meteorological variations, such as during the presented creep tests. Among the various warping modes, only the ones that locally distort the beam surface may involve an out-of-plane displacement. It is mostly the case of cupping, that happens in plain sawn lumber, and its effect should be given particular

attention. Moreover, a calibration target misplacement may happen due to operator's error and also create an out-of-plane motion.

The effect of wood cupping on shrinkage-swelling measurement is represented in Figure 8. The 4 markers of the calibration targets always remain in the same plane because they are stuck onto a rigid aluminium object, but there is no possibility to have them in the same plane as all the beam's markers. However, the homography process projects all markers into the real world distances as if they were in the same plane as the calibration target.

The error due to such out-of-plane displacement can be estimated geometrically. Let define  $d$  as the out-of-plane displacement,  $D_1$  and  $D_2$  the distances between the camera and two markers on the beam,  $H_{p1}$  their distance projected in the window target plane,  $H_{p2}$  their real distance. According to the intercept theorem (Figure 8b):

$$\frac{D_1}{H_{p1}} = \frac{D_1 + d}{H_{p2}} \quad (3)$$

where  $H_{p1} = H$ ;  $H_{p2} = H + er$ ,  $D_1 = D_2 = D$  and  $er$  is the location error coming from the out-of-plane motion. As the relative error is the error over the theoretical value, the result is divided by  $H$ . It leads to :

$$\frac{er}{H} = \frac{d}{D} \quad (4)$$

This result remains valid for any view angle.

The out-of-plane displacement due to wood cupping is a slow process depend-

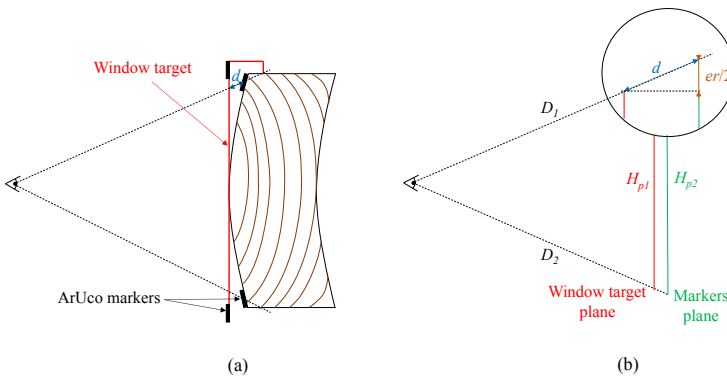


**Fig. 8** Effect of wood cupping on the shrinkage-swelling measurement of a beam: (a) illustration of the out-of-plane displacement ; (b) application of the intercept theorem.

ing on drying speed. If the calibration target is always placed in the same position, which was the case, then this displacement becomes a systematic error. This error is discarded when focusing on shrinkage-swelling variations. It would matter when analysing long-term variations, but as the studied beams

started with high moisture content, the long-term shrinkage-swelling overwhelmed this systematic error.

Nevertheless the out-of-plane displacement induces also a random error when positioning the calibration target. A realistic upper bound for operator's target placement error during the creep test is  $d = \pm 1$  mm, leading to a 0.2% error for  $D = 1000$  mm.

## 2.4 Guidance for success and accuracy

It is very important to keep a large white space around the markers. A black line too close to the edge of the ArUco pattern would disturb the marker detection.

During the first campaign there were problems during the markers detection process because of black cut lines close to the pattern.

The problem was overcome by reducing the photos quality to  $1000 \times 667$  pixels, only where it was needed. It is supposed that reducing the photo quality decreases the impact of the black lines relative to the whole pattern.

Obviously, using a tripod decreases significantly the random dispersion of a measurement. Its impact was estimated by taking 60 photos with a tripod and 60 photos without a tripod of the same paper sheet Figure 3 with the Canon camera. The results showed a 4 times lower standard deviation for the tripod measurements.

# 3 Results and discussion

## 3.1 Precision

### 3.1.1 Effect of distance between camera and markers

Figure 9 shows the evolution of the error, the relative error and the standard deviation with the distance between camera and markers. The error corresponds to the difference between real and measured values, where a real value is the distance between markers taken as input for the printer and checked with a ruler after the printing, and a measured value the distance computed using the photos of the paper sheet. The relative error corresponds to the error divided by the real value, i.e. 40 mm for dy12 and 175 mm for dy34, and the standard deviation refers to the measured distance obtained from five pictures. Obviously, the relative error of the x distance cannot be calculated because the real value is 0. The distance between the camera and the markers influenced both the size of the marker and its position in a photo.

It may be noted that:

- The distance had no observable impact on the error and very little on the relative error;
- The standard deviation increased with the camera-markers distance. This may be explained by the marker size reduction. For the 60 cm distance the

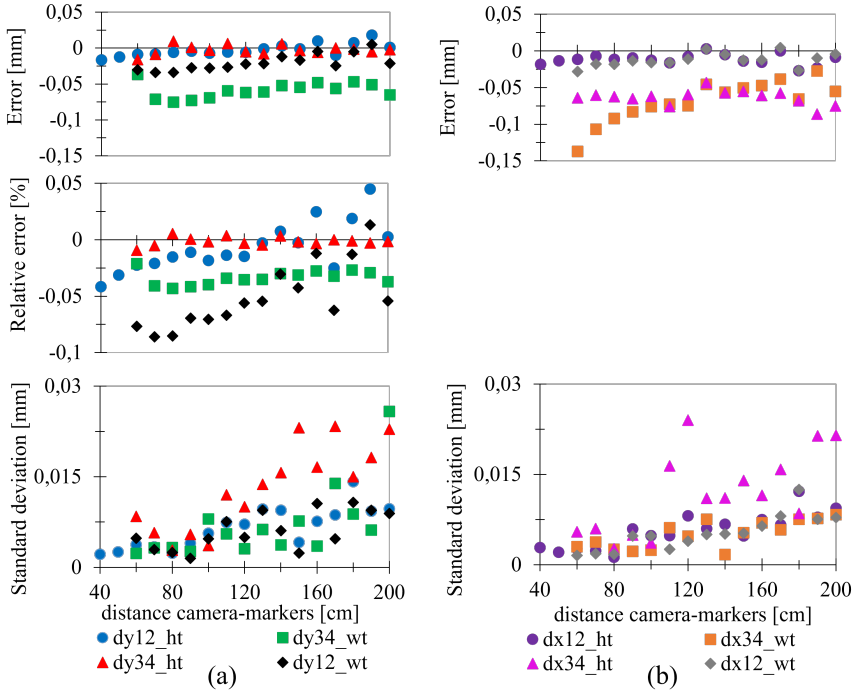


**Fig. 9** The impact of the distance between camera and markers: (a) error: difference between real and measured distance, relative error: error divided by real distance, and standard deviation of measured distance on ten photos for the y distances; (b) error, standard deviation for the x distance. dy12 and dy34 are the y distance between markers 1-2 (40 mm) and 3-4 (175 mm), respectively; dx12 and dx34 are the x distance between markers 1-2 (0 mm) and 3-4 (0 mm), respectively. Calibration target used for the homography: ht, horse-shoe target; wt, window target. Gray scale: diffgray = 156, mingray = 29, maxgray = 201.

markers were around  $250 \times 166$  px while for the 200 cm distance they were around  $80 \times 53$  px, thus reducing the detection precision.

The error associated with the distance between the camera and the markers was at most 0.08 mm.

### 3.1.2 Effect of angle

Figure 10 shows the evolution of the error, the relative error and of the standard deviation of the ten measurements, for an increasing horizontal angle.

Similar results were obtained for the vertical angle. It may be noted that the error associated with the 90 cm distance camera markers of these pictures has been corrected for the values (Figure 10). The view angle had no impact on the standard deviation of a series of photos. However, it increased the error especially in the considered direction: error on dy increased with the horizontal angle and error on dx increased with the vertical angle. This was particularly true for the large distances (dy34), as if the measured distance of 175 mm was

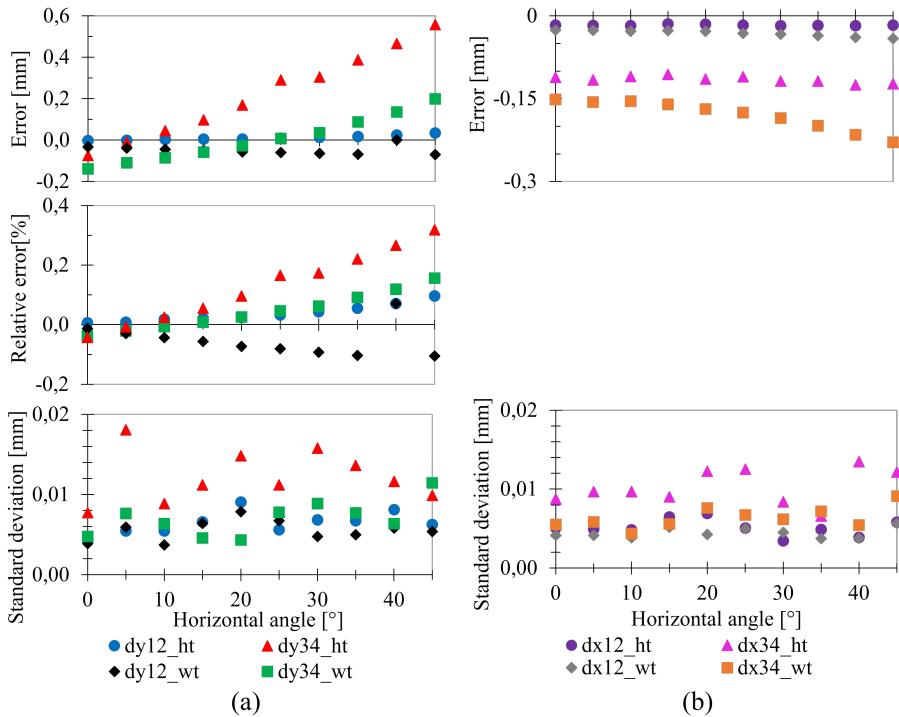


**Fig. 10** Impact of a horizontal angle: (a) error, relative error and the standard deviation on the y distance; (b) error and standard deviation on the x distance. The caption is the same as for Figure 9. Gray scale: diffgray = 164, mingray = 35, maxgray = 216.

reduced with the augmentation of the view angle. The depth of field could have been the reason, as some markers were less sharp than others, but in this case an error would have appeared for the x distance measurements, and the standard deviation would have increased. Possibly the homography result was imperfect due to the low number of markers used for the matrix calculation. New trials with more than 4 markers for the homography is a perspective to solve that problem. The relative error can reach 0.3% in inappropriate conditions, such as a large distance measured with a small calibration target (dy34\_ht). Otherwise (dy12\_ht, dy34\_wt, dy12\_wt), it remains below 0.2% and even below 0.08% as long as the view angle is kept lower than 25°.

### 3.1.3 Discussion on the precision tests

The precision tests confirm that choosing a Single Lens Reflex camera instead of a cheap smartphone camera does decrease the dispersion of the photo measurement. When measuring a distance between markers 175 mm apart, the results suggest to use the window target (Figure 10). Both the view angle and the camera-marker distance are random errors. The view angle has more impact on the precision and should be as close to 0 as possible. Only dy12\_ht,

dy34\_wt and dy12\_wt results are relevant to the situation encountered in the creep tests. The conditions of the creep tests photos were usually close to 90 cm for the camera-marker distance and the angle between 0 and 25°, that is a relative error lower than 0.08%; at which must be added the out-of-plane error presented in section 2.3.3, that is a relative error lower than 0.2%. This leads to an estimated total error majored by 0.28%. It corresponds to an error of 0.112 mm for the 40 mm distance and of 0.5 mm for the 175 mm distance. Nevertheless, other potential errors like the lightening conditions and camera parameters are not considered.

As a comparison, Malbezin et al. found an increase of the camera pose estimation error when the angle increases in the considered direction [9]. Moreover, Bremand et al. showed that during a marker tracking process, the smaller the marker, the bigger the standard deviation of its location [1]. Finally, Abawi et al. found that the distance between the camera and the target increases the standard deviation and the error of a pose estimation [10]. But they also found that the angle reduces the error especially between 30 and 40°, contrary to the observations of this study.

## 3.2 Results on creep tests

### 3.2.1 Measurement of transverse expansion

Figure 11 shows, for two beams of the second campaign, the correlation between the local transverse expansion near the notch and in the core of the beam where the whole height was measured (Figure 7). The expansion near the notch was computed using the markers of the crack opening in-between crack propagation events. The results are given as a fraction of the initial distance, so that they can be compared.

The results show a good correlation between the two measurements of trans-

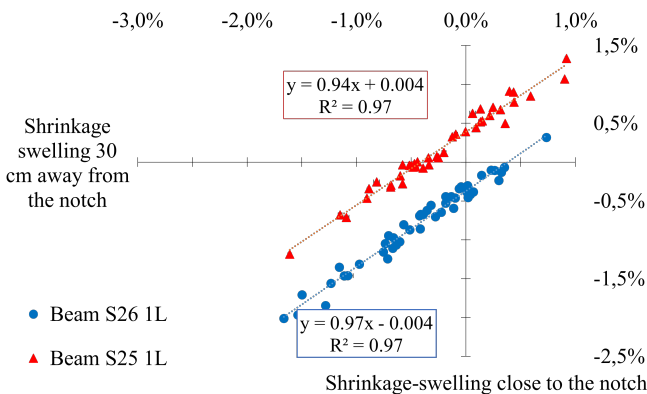


**Fig. 11** Correlation between transverse expansion at different locations. Beam S25 and S26 are considered on face 1 on the left. Gray scale: diffgray = 142, mingray = 13, maxgray = 253

verse expansion, with the value at the notch slightly higher than that measured

in the middle of the beam. The transverse shrinkage-swelling rate of wood is about 0.2 to 0.3 %/% [11], which at least corresponds to 0.35 mm of variation for 1% of moisture content change and with an initial distance of 175 mm. As the precision estimated is 0.28%, a variation of 1% of moisture content may not be identified. Nevertheless, a variation of more than 1%, such as the long-term shrinkage-swelling observed during the creep tests, should be identified. The correlation between both transverse expansions in Figure 11 is very good and the slope slightly lower than 1 may be explained by variation of wood properties along the beam combined with a delay resulting from the diffusion process.

### 3.2.2 Measurement of crack parameters

Figure 12a shows the crack opening of a beam subjected to crack propagation during the first campaign. The evolution of wood equilibrium moisture content (EMC) corresponding to the external climate is added in order to indicate whether the beam tends to shrink or to swell, as this should have an impact on the crack opening measurement. The EMC was computed using the Merakeb-Pedersen model ([12], [13]) that takes as inputs the previous moisture content, the outside temperature and relative air humidity measured with a weather station close to the experiment.

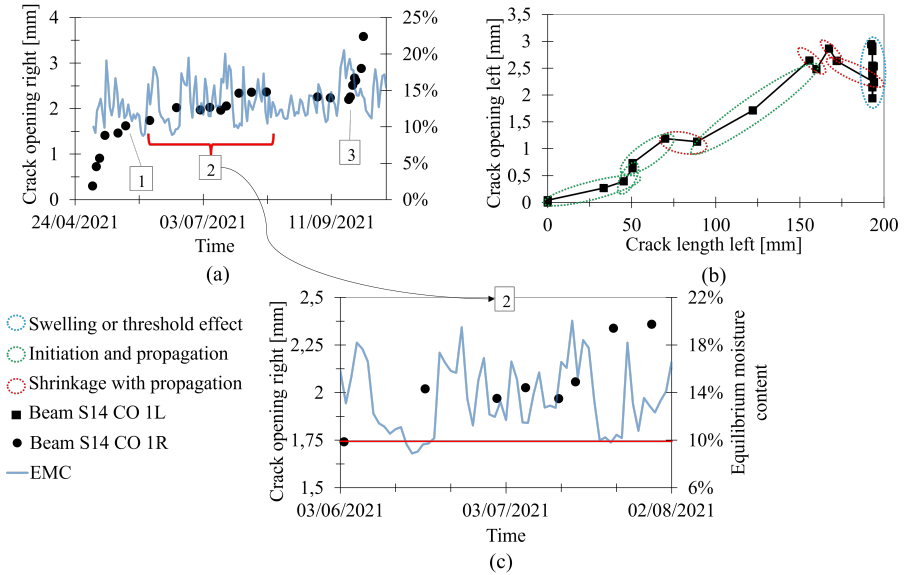
A rapid increase of crack opening is observed at the beginning of the test, after the initial loading, then again at the end of the 4-months period when additional loads are applied. Figure 12c focuses on an intermediate 2-months period, where the crack opening seems to be triggered by drying phases, since a significant increase is observed each time EMC falls below 10%. Note that the rupture eventually occurred on the left side of the beam, while the data shown are those of the right side.

Figure 12b shows the relationship between the crack opening and the crack length.

Three types of propagation are identified:

- Initiation and propagation, both CO and CL increase;
- Shrinkage with propagation, CO decreases because of the shrinkage but CL increases due to crack propagation. Maybe the crack propagation is only on the surface, which would explain why CO does not increase with CL;
- Swelling or apparent threshold effect, CL is constant but CO increases. It could be either due to the swelling of the beam or due to a threshold effect before crack propagation as identified by [14]. The threshold effect may be explained by the heterogeneity of the wood, if a knot is in the crack trajectory it would stop its propagation while the crack opening continues to grow.

The final CL after the beam cracked is not represented in the graph but reached 1290 mm. The results showing that the shrinkage helps the crack



**Fig. 12** Evolution of the crack parameters for beam S14: (a) simultaneous evolution of crack opening right side and daily mean wood equilibrium moisture content (EMC) during 4 months, where zone 1 is the end of the primary creep, zone 2 the 2 months concerned by (c) and zone 3 is the start of the daily load increase; (b) crack opening as a function of crack length, both left side; (c) time evolution of crack opening right side focused on 2 months. Gray scale: diffgray = 140, mingray = 9, maxgray = 252.

to propagate are in line with another similar experimental study ([14]) that identified the same phenomenon. Moreover, Figure 12b shows a crack opening varying from 0 to 3 mm and a crack length varying from 0 to 1290 mm, to be compared with those of that previous study, a crack opening between 0 and 3 mm and a crack length between 0 and 800 mm. Finally, a crack propagation of silver fir wooden beams is characterised by an increase of the crack opening of 0.3 mm minimum and an increase of the crack length of at least a few centimeters. 0.3 mm corresponds to 0.75% of the 40 mm markers distance, and the precision was majored by 0.28%. Therefore, for both the crack opening and the crack length the method is sufficiently reliable to identify the phenomenon as long as a correction is made for the thermal expansion of the calibration target.

## 4 Conclusion

The ArUco marker tracking technique presented in this article is flexible. Owing to the homography procedure, it enables to take photo with view angles and with different camera locations while maintaining a low error.

This advantage was useful in the context of the creep test where the experimental conditions were not suitable for other optical methods. The method also allows to compute distances between markers in a wide variety of ranges without additional effort. For example, the markers may be stuck 20 mm apart as well as 500 mm apart. The limitation is that all markers have to be in the same picture, the precision then comes from the number of pixels. On this subject, the marker tracking is more flexible than the LVDT sensors or transducers that have a fixed measuring range, so that it is necessary to consider what the LVDT sensor will be used for before purchasing it.

The financial cost of the method is attractive. The most expensive necessary device is the camera. A much better accuracy is obtained with a good SLR camera rather than with a smartphone. The markers just need to be printed on regular paper or cardboard and protected, for example with a matt lamination. A piece of metal is a good solution to have a reference calibration target for the homography. A computer is obviously necessary as well. Once the camera has been acquired, the number of measurements can be increased at no additional costs.

The method is quite simple to use as all the important functions are already programmed by the OpenCV community. Basic skills on python are necessary to adapt the use of the function to a specific case. The algorithms can be self-taught and for free with OpenCV and their community.

The precision of the method was estimated considering the out-of-plane displacement, the impact of a view angle and of the distance camera-markers. The most significant relative error may come from the out-of-plane displacement, it was geometrically determined that it can reach 0.2% due to calibration target misplacement. Then experimental results showed that the view angle had more impact on the measurements than the camera-markers distance. Under suitable conditions, i.e. a view angle of less than 25°, the relative error was below 0.08%. The total relative error is hence majored by 0.28%. The printed markers must have a large white space around the corners in order to ensure a good detection. Furthermore, they should be protected and stuck to a rigid body.

As an application examples, the ArUco markers tracking method have been used to measure the crack parameters and the shrinkage-swelling of wooden beams subjected to multi-steps creep tests. The results of the measurements made with the method are consistent with the physical phenomenon involved. Firstly, an increase of the crack propagation due to wood shrinkage of the beam was identified. Secondly, a good correlation between the transverse expansion of the beams in two different locations was obtained.

Other parameters probably impact the precision of the method but have not been estimated, for example picture brightness and camera parameters. The out-of-plane error analysis may be developed in case of wood application by computing the theoretical cupping of wood based on its growth rings. Moreover, it would be interesting to estimate the impact of the view angle when the homography is computed with more than 4 markers.

## 5 Acknowledgements

The authors would like to thank the Auvergne Rhône-Alpes region for the Ph.D. scholarship as well as the funding of the Hub-Innovergne program of the Clermont Auvergne University. Moreover, the method could only be developed thanks to the significant contributions of the OpenCV community. Finally the authors thank Benoît Blaysat for lending equipment and fruitful discussions.

## 6 Compliance with Ethical Standards

On behalf of all authors, the corresponding author states that there is no conflict of interest.

## Appendix A Homography

The aim of the homography is to project the coordinates in a given plane into another, as illustrated in Figure A1 coming from [15]. In the left picture the photo is taken with a view angle and on the right picture it is projected onto the plane parallel to the wall.

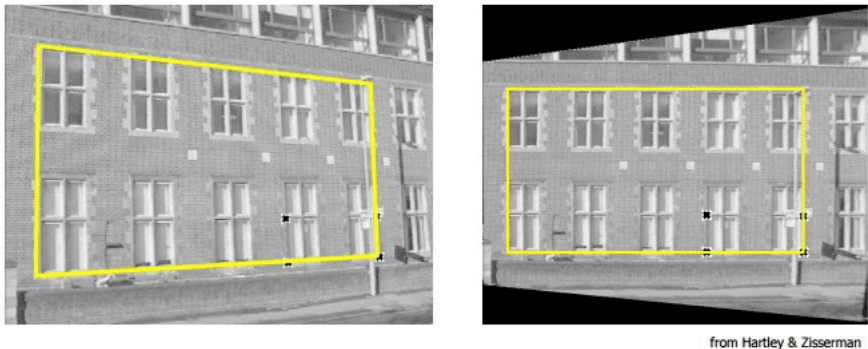


**Fig. A1** Left picture: view of a wall from an angle; right picture: transformed view of a wall to look like as if the camera were standing right in front of it.

In this study, the goal is to go from the virtual image plane to the physical real world plane, where the real distance between two markers is defined by their coordinates. The `detectMarkers` function of OpenCV returns the position of the markers into the 2D image coordinates (i.e., in pixels). In order to get real world coordinates (i.e., in meters), a homography must be computed:

$$\underline{X} = \omega \underline{H}.x$$

Where:

- $\underline{X} = (X, Y, Z)$  are the real world coordinates;

- $\underline{x} = (x, y, 1)$  are the homogeneous 2D image coordinates, related to the projective space. When passing from the Euclidean coordinates to the homogeneous coordinates, a dimension is added. This distance is fixed to 1 and allows to get mathematical coherence;
- $\underline{\underline{H}}$  is the  $3 \times 3$  homography matrix:

$$\underline{\underline{H}} = \begin{bmatrix} h_{11} & h_{12} & h_{13} \\ h_{21} & h_{22} & h_{23} \\ h_{31} & h_{32} & h_{33} \end{bmatrix} \quad (\text{A1})$$

- $\omega$  is a scale factor. In homogeneous coordinates,  $(x, y, 1)$  and  $(\omega x, \omega y, \omega)$  represent the same point for  $\omega$  a non-zero scalar. It may be fixed at  $\omega = \frac{1}{h_{33}}$  and injected into  $\underline{\underline{H}}$ . In this case let's note:

$$\tilde{h}_{ij} = \frac{h_{ij}}{h_{33}}, \quad (i, j) = ((1, 2, 3), (1, 2, 3))$$

The transformation needed to get the homogeneous 2D real-world coordinates is:

$$\hat{X} = \begin{pmatrix} X/Z \\ Y/Z \\ 1 \end{pmatrix} = \begin{pmatrix} \hat{x} \\ \hat{y} \\ 1 \end{pmatrix} = \frac{X}{Z} \quad (\text{A2})$$

It becomes:

$$\hat{X}.Z = \underline{\underline{H}}.x$$

For a given point the equations are:

$$\begin{cases} \hat{x}.Z = \tilde{h}_{11}x + \tilde{h}_{12}y + \tilde{h}_{13} \\ \hat{y}.Z = \tilde{h}_{21}x + \tilde{h}_{22}y + \tilde{h}_{23} \\ Z = \tilde{h}_{31}x + \tilde{h}_{32}y + 1 \end{cases}$$

Thus:

$$\begin{cases} \hat{x}.(\tilde{h}_{31}x + \tilde{h}_{32}y + 1) = \tilde{h}_{11}x + \tilde{h}_{12}y + \tilde{h}_{13} \\ \hat{y}.(\tilde{h}_{31}x + \tilde{h}_{32}y + 1) = \tilde{h}_{21}x + \tilde{h}_{22}y + \tilde{h}_{23} \end{cases}$$

By transforming  $\underline{\underline{H}}$  into a vector, the following equation can be written:

$$\begin{pmatrix} x & y & 1 & 0 & 0 & 0 & -x\hat{x} & -y\hat{x} & -1 \\ 0 & 0 & 0 & x & y & 1 & -x\hat{y} & -\hat{y} & -1 \end{pmatrix} \cdot (\tilde{h}_{11}, \tilde{h}_{12}, \tilde{h}_{13}, \tilde{h}_{21}, \tilde{h}_{22}, \tilde{h}_{23}, \tilde{h}_{31}, \tilde{h}_{32}, 1)^T = \begin{pmatrix} 0 \\ 0 \end{pmatrix} \quad (\text{A3})$$

Basically:

$$\underline{\underline{A}}.\tilde{\underline{H}} = \underline{\underline{0}}$$

Solving this problem, avoiding  $\tilde{\underline{H}} = \underline{\underline{0}}$ , is the homography computation. It is a minimization problem as the solution is never perfect for images obtained experimentally. It is worth noting that 1 point in a picture with known real-world positions gives 2 equations, and the homography matrix consists of 8

unknowns. As a consequence, at least 4 points with known physical positions are necessary to compute the homography matrix. These 4 points may be the 4 corners of a single marker, or as in the case of this study 4 centers of 4 markers. There is at least two reasons for using 4 centers of 4 markers instead of 4 corners of a single marker:

- The centers are more precisely located than the corners;
- The projection of the pixels in the physical real world plane is globally better with 4 centers rather than 4 corners. Indeed, the projection with 4 corners is good mainly around that reference marker but not for remote pixels.

Obviously, 3 collinear points give a useless redundant equation, so that no more than two should be aligned. If more than 4 points are available, the homography solution should give a better minimization.

The homography used to get real world coordinates of a given picture is the same for all markers. Thus, they are all projected on the same plane. As a consequence, the homography has to be computed one time for each photo so that the distance between two markers is correctly computed even with a view angle involving a perspective.

## References

- [1] Brémand, F., Cottron, M., Doumalin, P., Dupré, J.-C., Germaneau, A., Valle, V.: Mesures en mécanique par méthodes optiques. *Techniques de l'ingénieur*, 28 (2011)
- [2] Bornert, M., Brémand, F., Doumalin, P., Dupré, J.-C., Fazzini, M., Grédiac, M., Hild, F., Mistou, S., Molimard, J., Orteu, J.-J., Robert, L., Surrel, Y., Vacher, P., Wattrisse, B.: Assessment of Digital Image Correlation Measurement Errors: Methodology and Results. *Experimental Mechanics* **49**(3), 353–370 (2009). <https://doi.org/10.1007/s11340-008-9204-7>. Accessed 2022-03-02
- [3] Muñoz-Salinas, R., Marín-Jimenez, M.J., Yeguas-Bolivar, E., Medina-Carnicer, R.: Mapping and Localization from Planar Markers. arXiv:1606.00151 [cs] (2017). arXiv: 1606.00151. Accessed 2022-01-05
- [4] Germanese, D., Leone, G.R., Moroni, D., Pascali, M.A., Tampucci, M.: Long-Term Monitoring of Crack Patterns in Historic Structures Using UAVs and Planar Markers: A Preliminary Study. *Journal of Imaging* **4**(8), 99 (2018). <https://doi.org/10.3390/jimaging4080099>. Number: 8 Publisher: Multidisciplinary Digital Publishing Institute. Accessed 2022-01-05
- [5] Valença, J., Dias-da-Costa, D., Júlio, E., Araújo, H., Costa, H.: Automatic crack monitoring using photogrammetry and image processing. *Measurement* **46**(1), 433–441 (2013). <https://doi.org/10.1016/j.measurement>.

- 2012.07.019. Accessed 2022-03-23
- [6] Garrido-Jurado, S., Muñoz-Salinas, R., Madrid-Cuevas, F.J., Marín-Jiménez, M.J.: Automatic generation and detection of highly reliable fiducial markers under occlusion. *Pattern Recognition* **47**(6), 2280–2292 (2014). <https://doi.org/10.1016/j.patcog.2014.01.005>. Accessed 2021-08-30
  - [7] Forstner, Gulch: A fast operator for detection and precise location of distinct points, corners and centres of circular features. *Conference on Fast Processing of Photogrammetric Data*, 25 (1987)
  - [8] AFNOR: NF EN 408+A1 - Structures en bois. Bois de structure et bois lamellé-collé. AFNOR Editions (2012)
  - [9] Malbezin, P., Piekarski, W., Thomas, B.H.: Measuring ARToolKit accuracy in long distance tracking experiments. In: *The First IEEE International Workshop Augmented Reality Toolkit*, p. 2 (2002). <https://doi.org/10.1109/ART.2002.1107000>
  - [10] Abawi, D.F., Bienwald, J., Dorner, R.: Accuracy in optical tracking with fiducial markers: an accuracy function for ARToolKit. In: *Third IEEE and ACM International Symposium on Mixed and Augmented Reality*, pp. 260–261 (2004). <https://doi.org/10.1109/ISMAR.2004.8>
  - [11] Guitard, D.: *Mécanique du Matériau Bois et Composites*, Cépaduès edn. NABLA, vol. 1. Librairie Eyrolles, ??? (1987)
  - [12] Pedersen, C.R.: *Combined heat and moisture transfer in building constructions*. PhD thesis, Technical University of Denmark (1990)
  - [13] Merakeb, S., Dubois, F., Petit, C.: Modélisation des hystérésis de sorption dans les matériaux hygroscopiques. *Comptes Rendus Mécanique* **337**(1), 34–39 (2009). <https://doi.org/10.1016/j.crme.2009.01.001>. Accessed 2020-07-08
  - [14] Pambou Nziengui, C.F., Moutou Pitti, R., Fournely, E., Gril, J., Godi, G., Ikogou, S.: Notched-beam creep of Douglas fir and white fir in outdoor conditions: Experimental study. *Construction and Building Materials* **196**, 659–671 (2019). <https://doi.org/10.1016/j.conbuildmat.2018.11.139>. Accessed 2020-07-08
  - [15] Hartley, R., Zisserman, A.: *Multiple View Geometry in Computer Vision*, 2nd edn. Cambridge University Press, Cambridge (2004). <https://doi.org/10.1017/CBO9780511811685>. <https://www.cambridge.org/core/books/multiple-view-geometry-in-computer-vision/0B6F289C78B2B23F596CAA76D3D43F7A> Accessed 2022-01-13